



# Ore-forming processes of the Qixiashan carbonate-hosted Pb-Zn deposit, South China: Constraints from sulfide trace elements and sulfur isotopes

Wen-Dong Zhang<sup>a</sup>, Hai-Tao You<sup>a</sup>, Bin Li<sup>a,b,c,\*</sup>, Kui-Dong Zhao<sup>d</sup>, Xiao-Dong Chen<sup>a</sup>, Lei Zhu<sup>a</sup>

<sup>a</sup> Key Laboratory of Metallogenic Prediction of Nonferrous Metals and Geological Environment Monitoring (Ministry of Education), School of Geosciences and Information Physics, Central South University, Changsha 410083, China

<sup>b</sup> Deutsches GeoForschungs Zentrum (GFZ), Telegrafenberg, Potsdam 14473, Germany

<sup>c</sup> State Key Laboratory for Mineral Deposits Research, Department of Earth Sciences, Nanjing University, Nanjing 210093, China

<sup>d</sup> State Key Laboratory of Geological Processes and Mineral Resources, Collaborative Innovation Center for Exploration of Strategic Mineral Resources, Faculty of Earth Resources, China University of Geosciences, Wuhan 430074, China

## ARTICLE INFO

### Keywords:

Middle-Lower Yangtze River Valley

Carbonate-hosted deposits

Sphalerite

Trace elements

Sulfur isotopes

## ABSTRACT

The Middle-Lower Yangtze River Valley Belt (MLYRB) in South China contains many stratabound Fe-Cu-Pb-Zn deposits hosted in Middle-Upper Carboniferous carbonates. The origin and nature of the ore fluids are poorly constrained (syngenetic vs. epigenetic). Trace elements and sulfur isotope compositions of sphalerite and galena from the Qixiashan carbonate-hosted Pb-Zn deposit (Eastern of MLYRB) help to clarify the ore-fluid source and metallogenic processes. Three types of sphalerites have been distinguished (black sphalerite a, zoned sphalerite b and light color sphalerite c). High Fe and Mn contents of the early black sphalerite (Sp-a) were possibly derived from preceding Fe-Mn-rich sulfide layer or sediments from ore-bearing strata via replacement at 274–315 °C. The zoned sphalerite (Sp-b) has a dark Fe-Cu-rich core (321–348 °C) overgrown by a light Fe-Cu-poor rim (285–314 °C). The Sp-b rims are compositionally similar to Sp-a. Therefore, zoned Sp-b possibly represents the transition stage from poor copper (Sp-a) to rich copper (Sp-c) fluids. The light-color late sphalerite (Sp-c) is characterized by Fe-Mn depletion, as well as Ga, Cu, Cd and Sn enrichments. The Ga-rich Sp-c was possibly precipitated by the mixing of Ga-bearing sulfate and metalliferous fluid at 146–255 °C. We considered the Qixiashan Pb-Zn deposit to be of epigenetic origin that has undergone multistage ore-forming processes, in which the ore sulfur ( $\delta^{34}\text{S}$ : −3.7‰ to +7.8‰) was sourced from seawater sulfate (+22‰) via thermochemical sulfate reduction (TSR).

## 1. Introduction

Significant amount of global base metal sulfide resources are hosted in pelagic sedimentary rocks (Mudd et al., 2017). Many of these deposits are of sedimentary exhalative (SEDEX) type (Carne and Cathro, 1982), and some other sediment-hosted deposits were interpreted to be sub-seafloor replacement-type, e.g., Macmillan Pass in the Selwyn Basin (Canada) (Magnall et al., 2020). In this model, epigenetic hydrothermal ore-bearing fluids controlled the mass (e.g., Ba) transfer via replacement of preexisting sulfide or carbonate rather than hydrothermal venting.

Replacement is commonly reported to have formed sulfide laminae (Polito et al., 2006; Magnall et al., 2020; Rajabi et al., 2020). The diagenetic sediment dissolution and replacement by sulfides is proposed for the Irish-type (Wilkinson et al., 2015), MVT-type deposits (Corbella

et al., 2004), and the Red Dog district, Alaska) (Kelley et al., 2004). Recently, Liu et al. (2021) proposed that carbonate-buffered fluid mixing is critical for post-sedimentary Zn ± Pb ± Ba ore formation in carbonate rocks. The metal distribution and paragenesis by replacement occurred when acidic, oxidized ore fluids entered the pyrite-host lithology, allowing reduction and pH buffering by carbonate dissolution, resulting in stepwise metal deposition in an evolving fluid (Spinks et al., 2021). In addition, the mineral replacement reactions (coupled with dissolution-reprecipitation) could scavenge other ore-related metals/semi-metals, such as Bi, Au and U (Tooth et al., 2011; Li et al., 2015). Therefore, the contrasting genetic models (syngenetic vs. epigenetic) for sediment-hosted deposits imply different metal enrichment mechanisms.

Many sediment-hosted (Cu-Fe-Au, Mo, Zn, Pb, and Ag) deposits have

\* Corresponding author.

E-mail address: [cutelb@csu.edu.cn](mailto:cutelb@csu.edu.cn) (B. Li).

<https://doi.org/10.1016/j.oregeorev.2022.104786>

Received 25 August 2021; Received in revised form 13 February 2022; Accepted 16 February 2022

Available online 19 February 2022

0169-1368/© 2022 The Authors.

Published by Elsevier B.V. This is an open access article under the CC BY-NC-ND license

(<http://creativecommons.org/licenses/by-nc-nd/4.0/>).

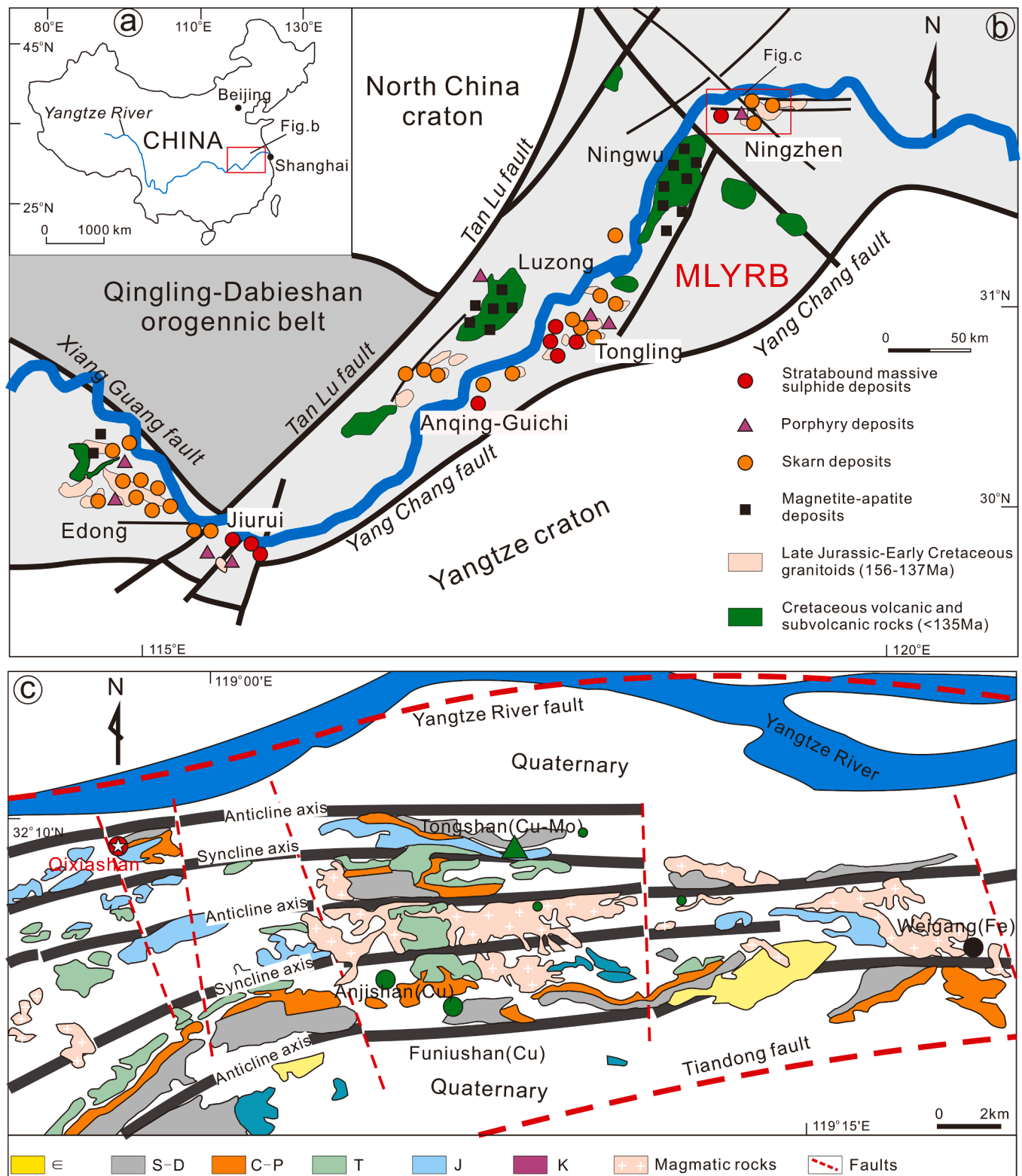


**Fig. 1.** (a) Schematic map showing the location of the Middle-Lower Yangtze River Metallogenic Belt (MLYRB), showing the distribution of (b) porphyry/porphyry-skarn deposits (modified after Pan and Dong, 1999; Mao et al., 2006) and (c) ore deposits in the Ningzhen orefield (modified after Zeng et al., 2013).

been discovered in the Middle-Lower Yangtze River Metallogenic Belt (MLYRB) in South China (Fig. 1a) (Pan and Dong, 1999; Mao et al., 2011; Pirajno and Zhou, 2015). Proposed genetic models include: 1) Late Carboniferous seafloor SEDEX (syngenetic) type (Xu and Zhou, 2001; Gu et al., 2007; Guo et al., 2011), as supported by the coeval mineralization (pyrite Re-Os age:  $319 \pm 13$  Ma) (Guo et al., 2011) with

the ore host at the Xinqiao deposit (Xu and Zhou, 2001; Zeng et al., 2002; Gu et al., 2007); 2) Early Cretaceous magmatic-hydrothermal origin (epigenetic) (Pan and Dong, 1999; Pirajno and Zhou, 2015), as supported by pyrite Re-Os ages of  $135.5 \pm 4.0$  Ma and  $136.7 \pm 4.6$  Ma (Li et al., 2018); 3) Carboniferous SEDEX ores overprinted by Cretaceous magmatic-hydrothermal mineralization (Gu et al., 2007; Zhou et al.,

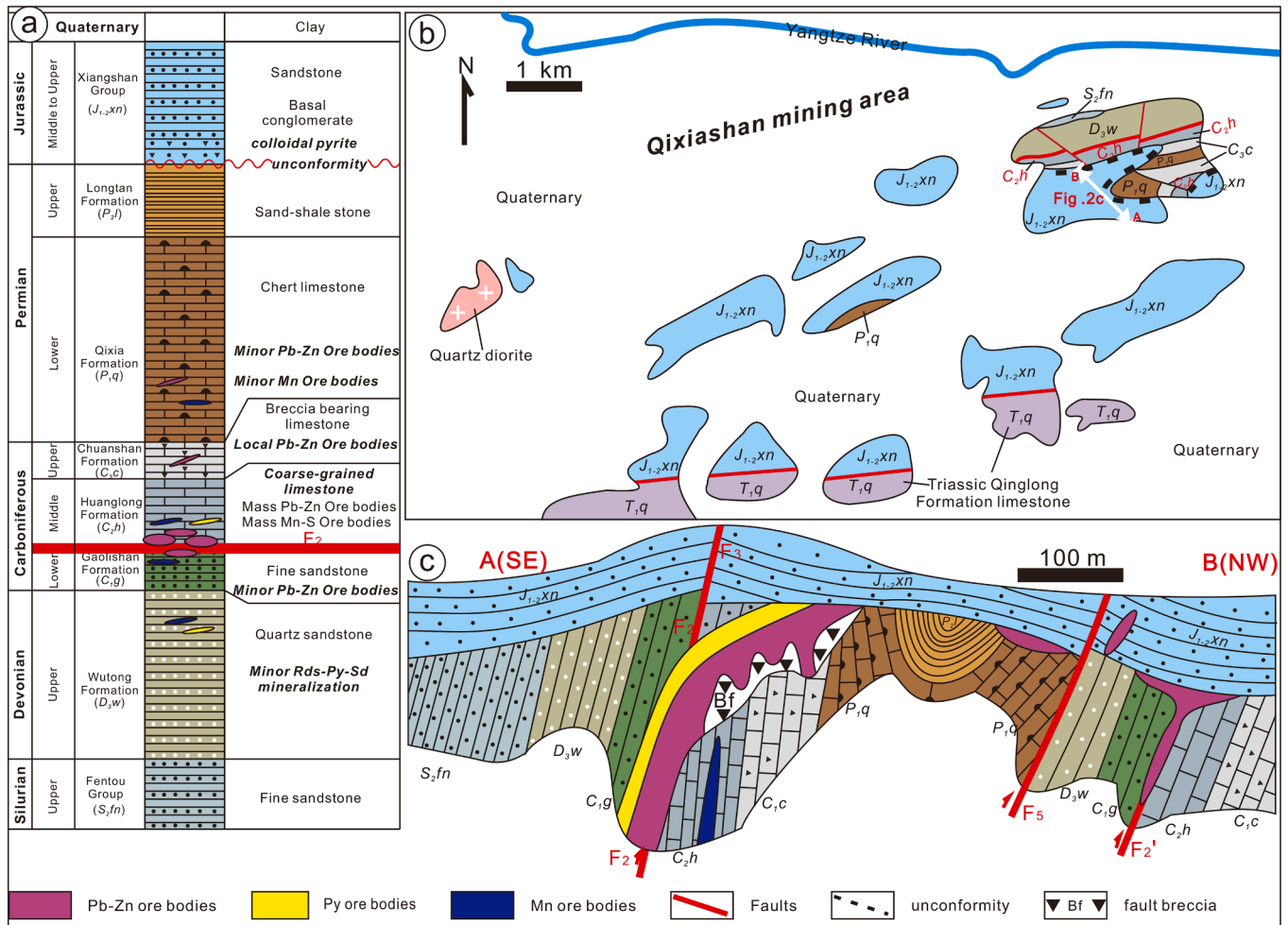


**Fig. 2.** (a) Generalized stratigraphic columns (modified after Gu et al., 2007) and (b) geologic map (modified after Sun et al., 2018) of the Qixiashan Pb-Zn-Ag-Mn deposit; (c) Cross-section of the Qixiashan deposit, showing the strata and orebodies (modified after Nanjing Yinmao Lead & Zinc Mining Co., 2016).

2015; Sun et al., 2018). Recent studies indicated that these deposits are predominately related to Cretaceous magmatic-hydrothermal systems, with additional contributions from Carboniferous rocks by water-rock interactions (skarn) (Li et al., 2018; Li et al., 2019). These base metal skarns have prograde skarn-type calc-silicate minerals (e.g., pyroxene and garnet), which are commonly reported in many skarn deposits in the region (Li et al., 2021).

Understanding the sulfur isotopes of ore sulfides would help to address issues such as the source, transport, and precipitation mechanism of sulfur, and has become an essential part of Pb-Zn mineralization research (Rye and Ohmoto, 1974). Integrating sphalerite trace element compositions and sulfur isotopes would provide a proxy for the origin and nature of ore fluids and ore-forming processes, which are dependent on changes in the fluid pH, temperature, redox, and compositions (Anderson, 1983; Corbella et al., 2004).

The Qixiashan Pb-Zn deposit in the MLYRB offers a good opportunity to investigate the trace element geochemistry of different types of sphalerites (e.g., marmatite, light-color unzoned and zoned sphalerite) from distinct hydrothermal environments with varying temperature, redox, and ore depositional processes. Here, we analyzed the trace element geochemistry (of sphalerite) and sulfur isotopes (of sphalerite and galena) through electron probe microanalysis (EPMA) and laser ablation inductively coupled plasma mass spectrometry (LA-ICP-MS) to determine the ore-forming mechanism (syngenetic vs. epigenetic), the variation trend of sulfide, and the ore-material source for the sediment-hosted deposits in the MLYRB.

## 2. Regional geology

The MLYRB is a regional depression on the northern margin of Yangtze Craton (Fig. 1b). It is bordered by the Qingling-Dabie ultrahigh-pressure (UHP) metamorphic belt and the North China Craton to the north, and is sandwiched the Yang-Change Fault to the south and the Xiang-Guang and Tan-Lu faults to the north (Pan and Dong, 1999) (Fig. 1b). The MLYRB consists of thick Cambrian-Triassic pelagic carbonate-clastic-evaporite successions, which overlie unconformably the Precambrian low-grade metamorphosed basement (Gao et al., 1999). The Jurassic-Cretaceous sequences comprise lacustrine- and swamp-facies sandstone, siltstone, and shale. The Lower Cretaceous sequence mainly consists of volcanic-clastic rocks, including mainly welded breccia, tuff, andesite, rhyolite, trachyte, and minor basalts. Extensive NE-trending faults and folds were developed in the Cambrian-Triassic sedimentary strata due to repeated tectonic activities (Pan and Dong, 1999). This environment was beneficial to the emplacement of the Jurassic to Cretaceous magmatic rocks, which intruded into the Cambrian-Triassic pelagic sedimentary rocks during the Late Mesozoic (Li et al., 2017). The extensive fault-fold system in the MLYRB controls the occurrence of the Late Paleozoic-Early Mesozoic sedimentation, the Jurassic-Cretaceous granitoid emplacement, and mineralization in the region (Fig. 1b).

The Late Jurassic-Early Cretaceous high-K calc-alkaline granitoids are widespread in the MLYRB, and are genetically associated with the Cu-Au-Mo-Fe-Pb-Zn-Ag mineralization in five orefields, i.e., (from west to east) the Ningzhen, Tongling, Anqing-Guichi, Jiurui, and Edong

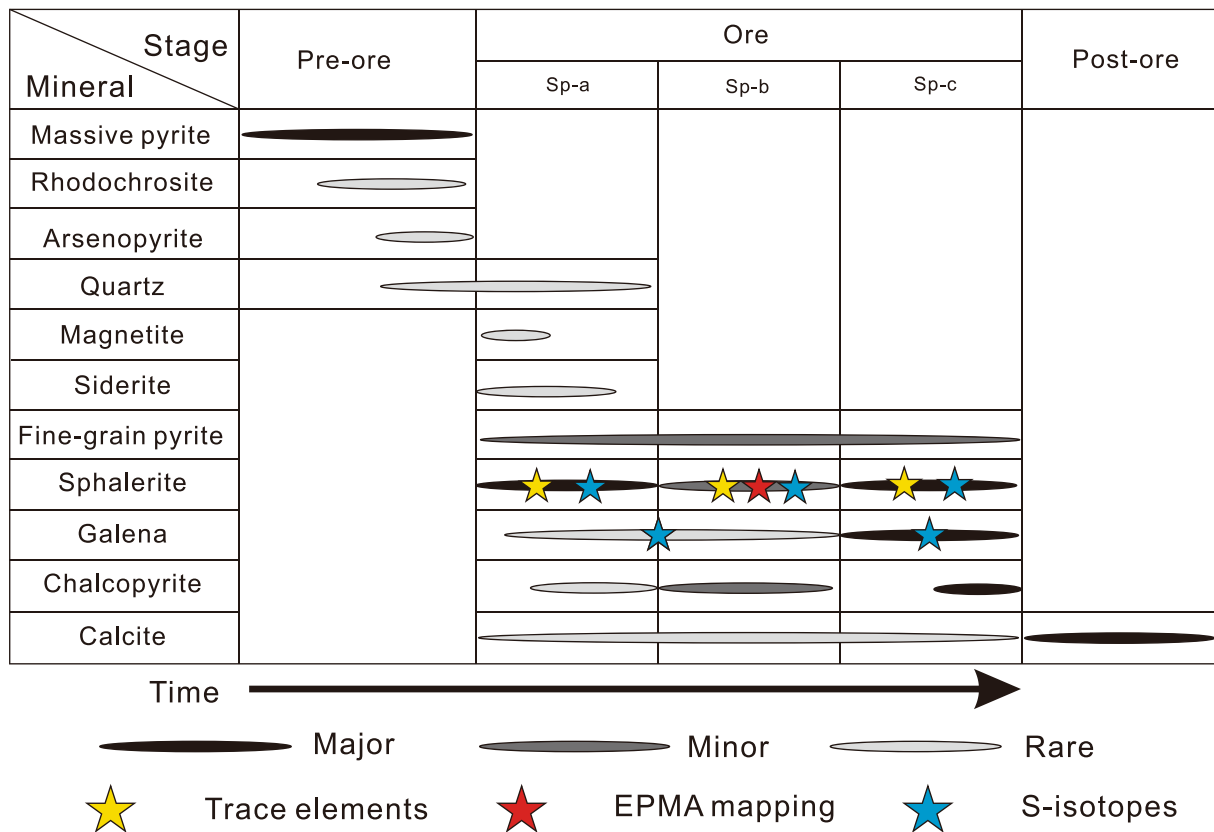


Fig. 3. Mineral paragenesis of the Qixiashan deposit.

(Fig. 1b) (Pan and Dong, 1999). The Early Cretaceous Fe skarn deposits are clustered in the subaerial Ningwu and Luzong volcanic basins (Mao et al., 2006; Zhou et al., 2015), and are associated with shoshonitic rocks. Four types of polymetallic deposits have been identified in the MLYRB based on their spatial-temporal distribution, metal association, and possible magmatic link (Fig. 1b) (Pan and Dong, 1999; Mao et al., 2006; Pirajno and Zhou, 2015; Zhou et al., 2015; Li et al., 2018): (1) porphyry-skarn Cu-Au-Mo deposits (e.g., the Chengmenshan and Tongshankou) related to Jurassic–Cretaceous granitoids (Li et al., 2010); (2) Fe-Cu skarn deposits (e.g., the Wushan and Tongguanshan) along the contact between the Jurassic–Cretaceous intrusions and the Upper Paleozoic–Lower Mesozoic carbonates; (3) iron oxide-apatite (IOA) deposits associated with shoshonitic porphyries; and (4) stratabound massive sulfide deposits (e.g., the Qixiashan and Xinqiao) in Upper Paleozoic–Lower Mesozoic pelagic carbonates (Sun et al., 2018; Li et al., 2018).

The Ningzhen orefield is located on the eastern MLYRB margin (Fig. 1a). EW- to NNE-trending folds, including three anticlines and two synclines, were developed in the Cambrian–Triassic pelagic sedimentary rocks in the orefield by the Indosinian (Triassic) orogenic movement (Fig. 1c) (Zhang et al., 2017). The Cambrian–Triassic pelagic sedimentary rocks are unconformably overlain by Jurassic–Cretaceous continental volcanic-sedimentary rocks (Zhang et al., 2017). The Qixiashan Zn-Pb sulfide mineralization is hosted by Carboniferous Huanglong Formation ( $C_2h$ ) shallow-pelagic carbonates intercalated with sandstone. Above that lies the Lower Permian Qixia Formation ( $P_1q$ ) chert-limestone, the Dalong Formation chert (which hosts the Tongshan Cu deposit), and the Qinglong Formation limestone-dolomite (which hosts the Anjishan Cu deposit) (Zhang et al., 2017; Sun et al., 2018). Similar to the other orefields in the MLYRB, porphyry/skarn Cu-Fe-Mo deposits in the Ningzhen orefield are also related to the Jurassic–Cretaceous magmatic rocks (Fig. 1c). These magmatic rocks were emplaced in two phases, including the earliest gabbro-diorite, and quartz diorite-

granodiorite-granite and rhyolite.

### 3. Ore deposit geology

Located in the western Ningzhen orefield (Fig. 1c), the Qixiashan Pb-Zn-Ag-Mn deposit contains ~2.6 million metric tonnes (Mt) of ore @ 13.38% Pb + Zn, 0.99 Mt Mn @ 18.88%, 7.83 Mt S, 35 t Au @ 0.95 g/t, and 1113.64 t Ag @ 107.75 g/t (Nanjing Yinmao Lead & Zinc Mining Co., 2016). Local stratigraphy comprises Silurian-Permian pelagic sedimentary rocks at the bottom and Jurassic terrestrial sedimentary rocks at the top (Fig. 2a). The Triassic Qinglong Formation limestone ( $T_1q$ ) is missing in the Qixiashan orefield, and is only found to the south of it (Fig. 2b). The Silurian-Permian pelagic carbonate-clastic rocks are unconformably overlain by the Jurassic Longtan Formation terrestrial volcanic-clastic rocks (Fig. 2). The Indosinian tectonism formed EW-trending faults and folds (anticlines) in the Silurian-Permian sequences. At Qixiashan, the stratabound mineralization formed at least four stacks of tabular/lensoidal massive sphalerite-galena-pyrite-rhodochrosite orebodies. The rhodochrosite-pyrite mineralization occurs as bands or breccias in the sandstone of the Upper Devonian Wutong Formation ( $D_3w$ ) and the Lower Carboniferous Gaolishan Formation ( $C_1g$ ), and in the limestone of the Huanglong ( $C_2h$ ) and Qixia ( $P_1q$ ) formations (Fig. 2a and c). The sphalerite-galena mineralization is hosted in the Huanglong Formation limestone and the Qixia Formation chert-limestone (Fig. 2a), with the latter containing ~95% of the Pb-Zn-Fe-Mn metal reserve (Fig. 3).

The Pb-Zn-Fe-Mn orebodies vary in thickness and grade, and is characterized by massive Zn-Pb ores surrounded by pyrite-rich altered rocks and rhodochrosite-bearing calcite (Sun et al., 2019). The ENE-trending fault ( $F_2$ ) (Fig. 2b) cuts the Gaolishan Formation ( $C_1g$ ), extending along the contact between the Gaolishan and Huanglong Formation (Fig. 2c), and hosts most of the Pb-Zn-Fe-Mn ores in a breccia zone. The  $F_2$  branches out as a new fault ( $F_3$ ), further cutting the basal



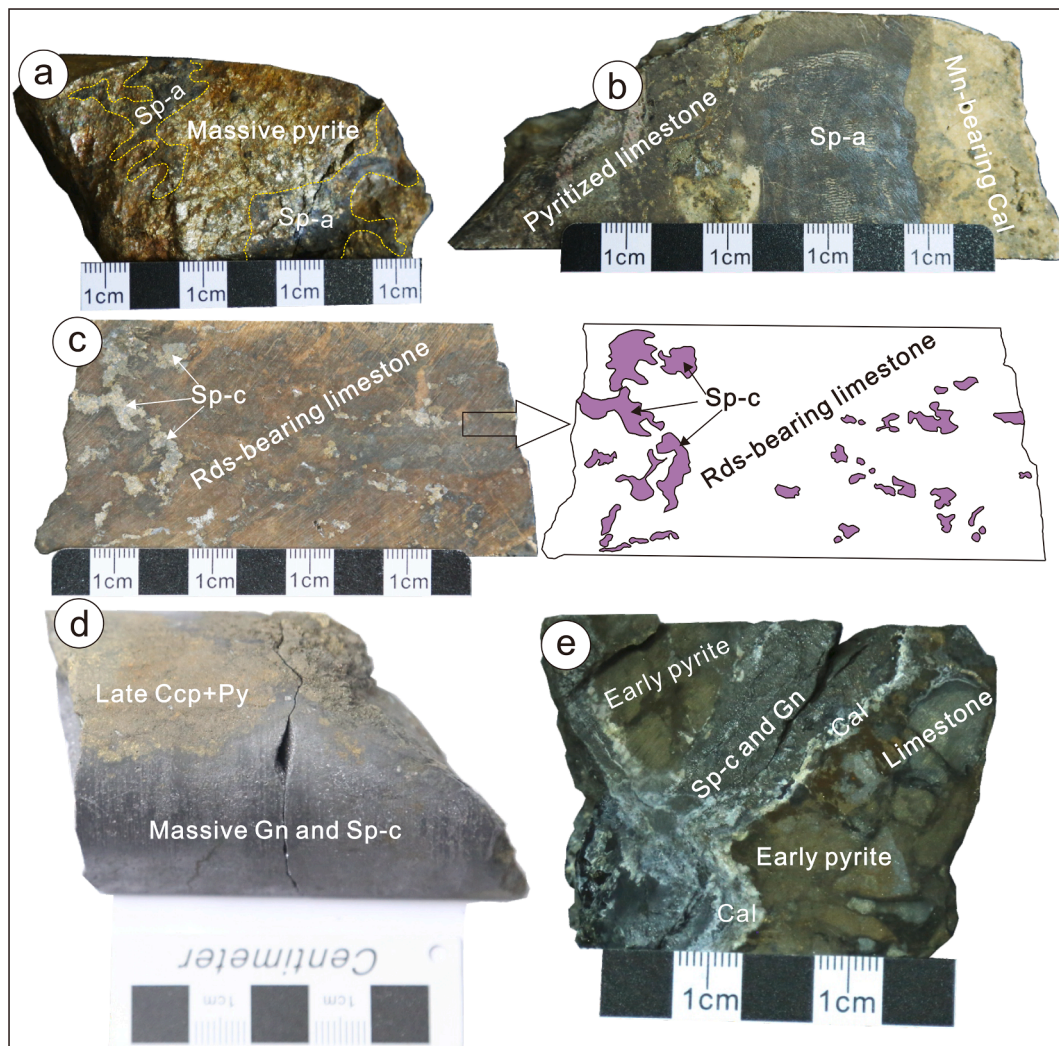


**Fig. 4.** Photographs of the Qixiashan sphalerite samples: (a) Black sphalerite (Sp-a) cut pre-ore massive pyrite (pre-ore Py); (b) Sp-a intercalated with pyritized limestone; (c) Disseminated light yellow sphalerite (Sp-c) in rhodochrosite (Rds)-bearing limestone; (d) Massive galena (Gn) and minor Sp-c; (e) Sp-c and galena veins with carbonate (Cal), replacement early sulfide and limestone breccia.

conglomerate and sandstone of the Xiangshan Group ( $J_{1-2}^{xn}$ ) (Fig. 2c).

The Pb-Zn-Fe-Mn ores consist mainly of sphalerite, galena, pyrite, and chalcopyrite, and minor rhodochrosite, siderite, magnetite, calcite, quartz, and barite. Three types/generations of sphalerites have been identified, i.e., (from early to late) (1) black Fe-rich sphalerite (Sp-a) intergrown with pre-ore massive/colloidal euhedral fine-grained pyrite and pyritized limestone (Fig. 4a and b), and is associated with minor galena, quartz, and siderite (Fig. 5a–d); (2) coarse-grained, core-rim zoned sphalerite (Sp-b), with black core surrounded by light rim (Fig. 5e). Chalcopyrite inclusions are widespread in the Sp-b core, clearly distinct from the clean Sp-b margin; (3) light yellowish-brown, Fe-poor sphalerite (Sp-c) has abundant galena and minor pyrite, and is disseminated in the rhodochrosite-bearing limestone (Fig. 4c). Sp-c also occurs as massive ore (Fig. 4d) and veins that cut the early pyrite and limestone (Fig. 4e). Anhedral Sp-c intergrown with fine-grained galena and pyrite (Fig. 5f, g), and shows “chalcopyrite disease”, which is distinct from the those in symbiosis with the coarse grain galena (Fig. 5f and g). Sp-c and co-precipitated pyrite tend to be fine-grained in the galena-dominated ore samples (Fig. 5h).

#### 4. Samples and methods

Sulfide (Sp-a, Sp-b, Sp-c and galena) samples were collected from

0 to 420 m depths of the Huzhuashan ore section at Qixiashan. Polished thin sections (30  $\mu\text{m}$ ) were examined under reflected/transmitted light and then analyzed for the major and trace element mineral compositions.

##### 4.1. EPMA major element analysis

The sphalerite and galena compositions were determined in the Central South University (China), on a Shimadzu EPMA-1720H microprobe equipped with wavelength- and energy-dispersive X-ray detectors and a backscatter electron (BSE) detector. Zoned sphalerite crystals were identified and major element mapping was performed on the same EPMA. Ga, Ge, In, Sn, Co, and Ni were not detected or below the detection limits. The X-ray lines for each element were as follows: S ( $K\alpha$ ), Zn ( $K\alpha$ ), Mn ( $K\alpha$ ), Cd ( $L\alpha$ ), Fe ( $K\alpha$ ), and Cu ( $K\alpha$ ). The element calibration standards used include: chalcopyrite (S, Fe, and Cu), metallic manganese (Mn), sphalerite (Zn), and greenockite (Cd). The minimum detection limits are: Cu (0.02 wt%), Fe (0.03 wt%), Zn (0.03 wt%), Cd (0.03 wt%), and Mn (0.04 wt%).

##### 4.2. LA-ICP-MS sphalerite trace element analysis

The analysis on the three types of sphalerite (Sp-a, Sp-b, and Sp-c)



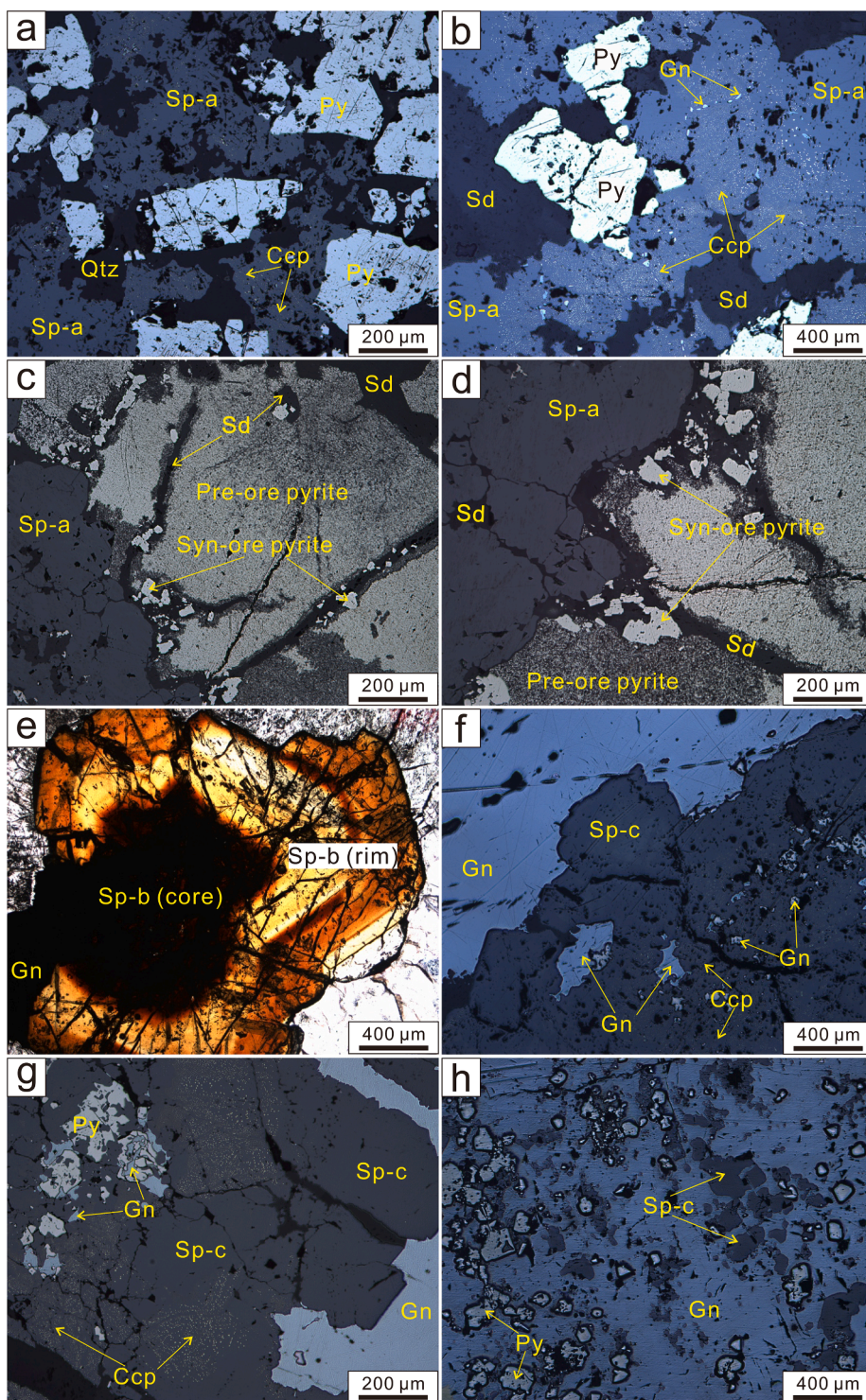


**Fig. 5.** Photomicrographs of the Qixiashan sphalerite samples: (a–b) Euhedral sphalerite (Sp-a) associated with minor pyrite and siderite with weak silicification; (c–d) Sp-a associated with minor co-precipitated siderite and euhedral fine-grained pyrite, crosscutting earlier pre-ore pyrite; (e) Zoned sphalerite (Sp-b) with chalcopyrite-bearing black core and light-colored rim; (f–g) sphalerite (Sp-c,) free chalcopyrite inclusions (Ccp) co-existing with coarse-grained galena (Gn), with abundant chalcopyrite inclusions co-precipitated with fine-grained galena and pyrite (Py); (h) fine-grained Sp-c and pyrite co-existing to coarse-grained galena.

was carried out at the Wuhan Sample Solution Analytical Technology Co. Ltd. (China). The laser sampling was performed using a GeolasPro laser ablation system consisting of a COMPexPro 102 ArF excimer laser (wavelength of 193 nm and maximum energy of 200 mJ) and a MicroLas optical system. Depending on the sphalerite grain size, the spot size of 44 and 32  $\mu\text{m}$  and laser frequency of 6 and 5 Hz, respectively, were used. The ionic signal intensity was obtained on an Agilent 7700e ICP-MS. Helium was used as the carrier gas (0.65 L/min) and argon as the make-up gas, with was mixed via a T-connector signal smoothing device before entering the ICP system (Hu et al., 2015). Glass reference

materials NIST 610 and NIST 612 were used for the external standard calibration (Liu et al., 2008). Mass-1 (USGS) was used as the monitoring standard sample to test the reliability of the calibration method, and the ICPMSDataCal software (Liu et al., 2008) was used for the blank signal selection and instrument sensitivity calibration.

#### 4.3. LA-MC-ICP-MS sulfur isotope analysis

The analysis on sphalerite and galena was conducted at the China University of Geosciences (Wuhan). A Renetics-S155 laser ablation

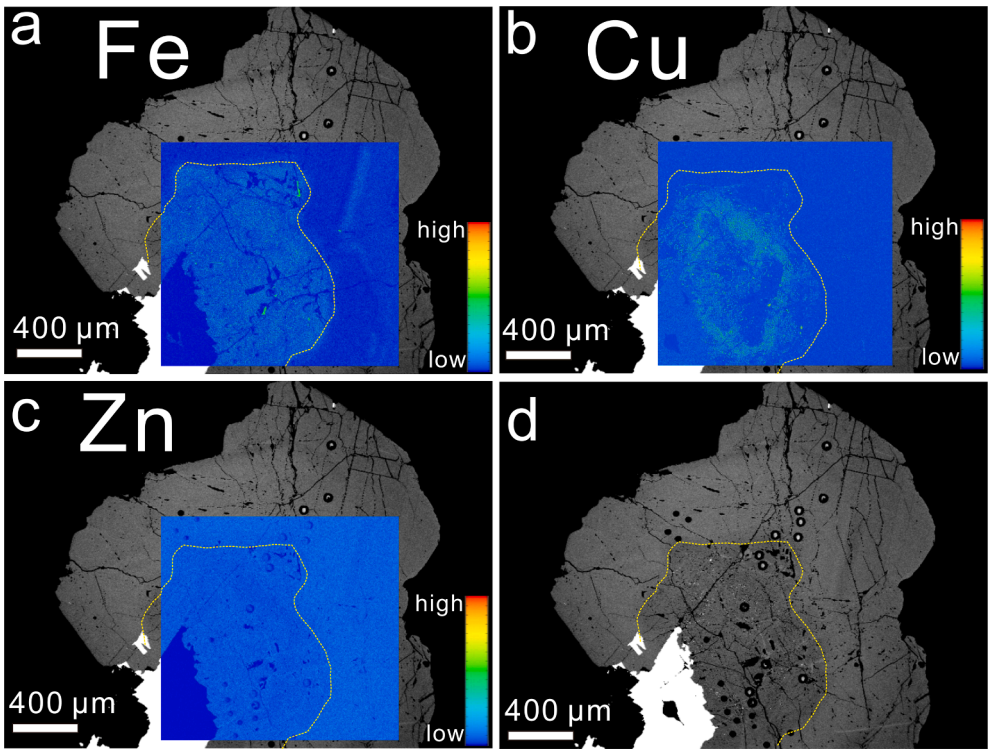


**Fig. 6.** EPMA element distribution maps of (a) Fe (b) Cu, and (c) Zn, and (d) BSE image of the zoned Sp-c, showing that the core has higher Fe and Cu but lower Zn contents than the rim.

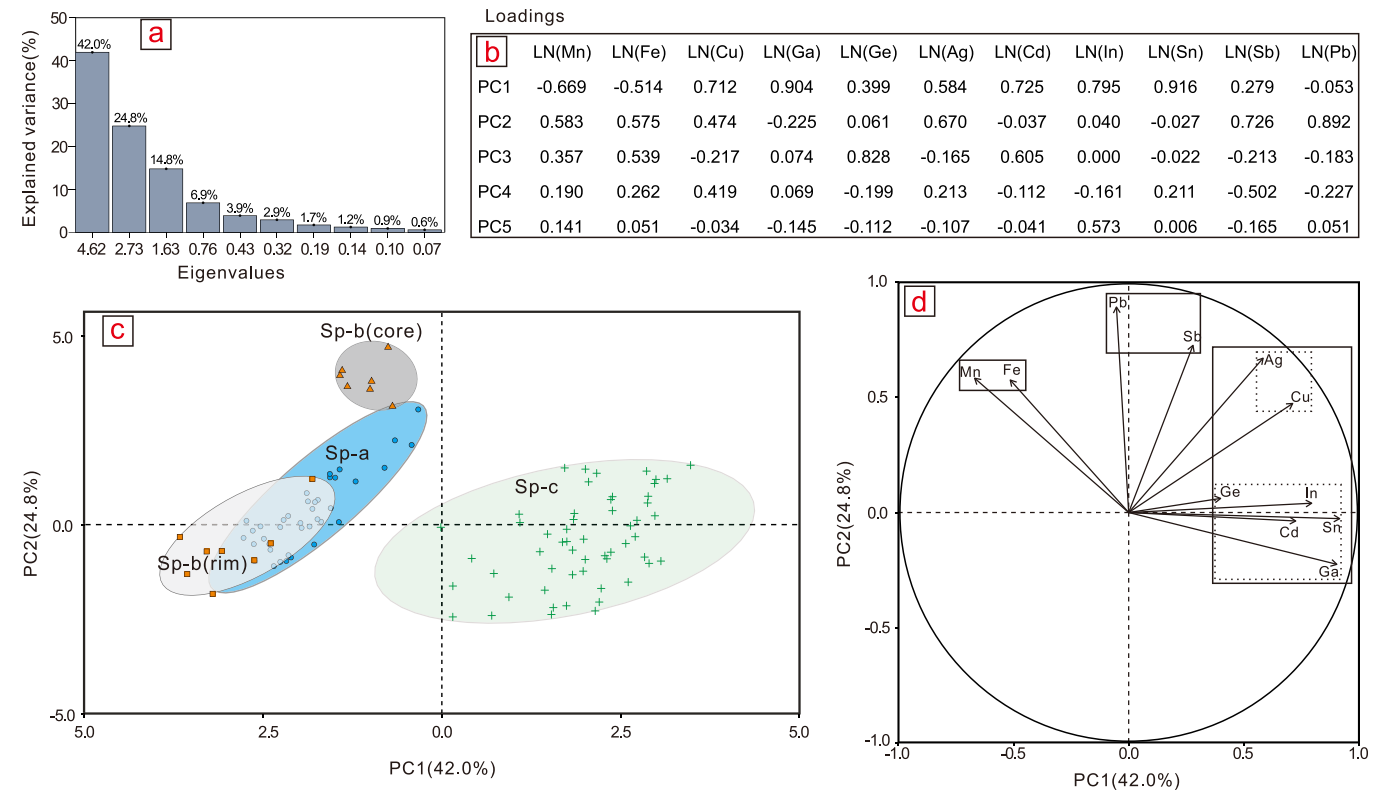


**Fig. 7.** PCA of the log-scale LA-ICP-MS trace element dataset of the Qixiashan sphalerite: (a) Scree plot of the Eigenvalues of correlation matrix; (b) Loadings of the principal components; (c) Score plot of all data points, and corresponding histograms of PC1 and PC2 for the trace element composition of the three types of sphalerites; (d) Loading plot of the PCA showing the elements (variables) and framed groups of elements with similar behavior.



**Table 1**

LA-ICP-MS and S isotope results for the sphalerite and galena.

	Sp-a		Sp-b (core)		Sp-b (rim)		Sp-c		Gn	
	Median	Range	Median	Range	Median	Range	Median	Range	Median	Range
Mn (ppm)	2749	2749–3946	4695	3206 – 5543	2324	919–3644	415	6.85–867	—	—
Fe(wt %)	4.28	4.28 – 8.11	53,244	4.53 – 5.74	1.76	1.46 – 3.37	11,559	117–16786	—	—
Cu (ppm)	19.8	19.8–577	22,214	9978 – 34,987	3.48	1.22 – 73.5	572	0.97–2557	—	—
Ga (ppm)	2.59	2.59 – 21.7	0.83	0.42 – 2.68	1.73	0.17 – 4.00	308	1.07–2589	—	—
Ge (ppm)	2.25	2.25 – 3.08	0.64	bdl – 1.42	0.66	bdl – 1.10	2.23	0.06 – 3.01	—	—
Ag (ppm)	4.18	4.18 – 15.4	152	34.9 – 203	1.34	0.94 – 6.23	9.73	0.22 – 69.7	—	—
Cd (ppm)	4263	4263–4740	2208	1891 – 2455	2555	3146–2888	6741	205–11214	—	—
In(ppm)	0.32	0.32 – 1.16	0.25	0.15 – 1.10	0.25	0.06 – 0.70	3.58	0.01–106	—	—
Sn (ppm)	0.52	0.52 – 21.3	3.44	1.76 – 257	0.72	0.28 – 1.10	366	0.01–2001	—	—
Sb (ppm)	0.93	bdl – 18.5	1.50	0.61 – 117	0.08	bdl – 13.8	0.66	bdl – 30.4	—	—
Pb (ppm)	1.74	1.74–170	69.8	15.6 – 398	1.02	0.36 – 9.00	0.80	bdl – 21.8	—	—
Mo (ppm)	0.24	0.24 – 0.38	0.04	bdl – 0.11	0.02	bdl – 0.07	0.08	bdl – 1.05	—	—
$\delta^{34}\text{S}$ (‰)	+3.3	+1.0 to +7.4	+5.3; +4.6	+3.1‰ to +5.6‰; +3.9‰ to +5.3‰	+6.4; +7.2	+4.2‰ to +7.5‰; +6.6‰ to +7.8‰	+2.5	–1.7 to +6.5	–0.7	–3.7 to 3.0

bdl: values below detection limits for trace elements (typically 0.01 ppm).

system was equipped with an ArF excimer laser generator to generate a 193 nm deep ultraviolet beam, which was focused on the sulfide surface through the homogenization path. Helium (0.65 L/min) mixed with argon (0.85 L/min) and nitrogen was transported into the Nu plasma II MC-ICPMS. The  $^{34}\text{S}/^{32}\text{S}$  ratios of the standard and unknown samples were calculated with the standard sample bracketing (SSB) method to obtain the  $\delta^{34}\text{S}$  values. The standard used were NBS-123 and IAEA-S-1. The laser beam diameter was set to 40–50  $\mu\text{m}$ , the frequency was 10 Hz, and the ablation time was 40 s. The true sulfur isotope ratio was obtained based on a linear interpolation between two adjacent standards, and by correcting for the instrument mass deviation. The analytical analysis accuracy ( $1\sigma$ ) was about  $\pm 0.1\text{‰}$ , and the data are reported in delta notation (‰) relative to Vienna Cañon Diablo Troilite (V-CDT).

#### 4.4. Principal component analysis

We use principal component analysis (PCA) to better interpret the minor-trace element data for the three types of sphalerite. To perform variable-reduction analysis from the high-dimensional data set (11

dimensions in this study: Fe, Mn, Pb, Sb, Ag, Cu, Ge, In, Cd, Sn and Ga), and to extract the main features that are more distinguishable for the three kinds of sphalerite, we took the top 2 principal components (PC1 and PC2, using the variance percentage in the total variance to indicate the importance) to represent the data set information. The few values that are below the detection limit (bdl) were replaced by their mean values. The raw trace element concentrations of Sp-a to Sp-c were further log-transformed before the PCA dimensional transformation analysis, and the PCA was performed in the R software environment.

## 5. Results

The results from EPMA ([Supplementary Table S1](#)) are consistent with those from LA-ICPMS. Sp-a has higher Fe (6.80–13.47 wt%) and Mn (0.12–1.07 wt%) concentrations than Sp-c (Fe: 0.84–6.85 wt%, Mn: 0.01–0.17 wt%). Sp-b has decreasing Fe and Mn contents from core (Fe: 4.82–10.37 wt%, Mn: 0.21–0.93 wt%) to rim (Fe: 2.46–5.30 wt%, Mn: 0.14–0.58 wt%). Minor element (Fe, Cu, Mn, Cd and Zn) mapping on Sp-b shows the same core-rim variation trend as obtained from the LA-ICP-

**Table 2**

Summary comparison between three types of sphalerite.

	Sp-a	Sp-b (core)	Sp-b (rim)	Sp-c	Gn
Assemblage	Crosscut massive Pyrite, associated with minor galena	Associated with minor galena and chalcopyrite disease	Associated with minor galena	Associated with fine-grained pyrite and numerous galena	Associated with fine-grained pyrite and sphalerite
Crystal size	Medium coarse grain	Coarse grain	Coarse grain	Fine to coarse grain	Fine to coarse grain
Morphology/texture in etched crystals	Anhedral crystals exhibit a black color	Black zonation exhibit porous corrosion associated with chalcopyrite disease	Brown zonation	Subhedral-xenomorphic crystals exhibit a light yellow color	Anhedral crystals occurs between sphalerite crystals
Enriched elements	Mn, Fe	Mn, Fe, Cu, Ag, Sb, Pb	Mn	Ga, Cu, Cd, Sn	—
Poor elements	Ga, Ge, In, Sn, Sb, Pb	Ga, Ge, In	Fe, Cu, Ga, Ge, Ag, In, Sn, Sb, Pb	Mn, Fe, Ge, Pb	—
Zonation pattern	Not found	Higher Cu, Fe in the core	Poor Cu Fe in the rim	Barren chalcopyrite disease Coexists with coarse galena contrasting with prevailing chalcopyrite disease associated with fine grain galena	Not found
S isotope	Slightly positive (+1.0 to +7.4)	Outward progressive $^{34}\text{S}$ enrichment from core to rim (Core: +3.1‰ to +5.6‰ and +3.9‰ to +5.3‰; Rim: +4.2‰ to +7.5‰; +6.6‰ to +7.8‰)		Slightly negative (–1.7 to +6.5)	Yield tightly range of $\delta^{34}\text{S}$ values (–3.7 to +3.0)



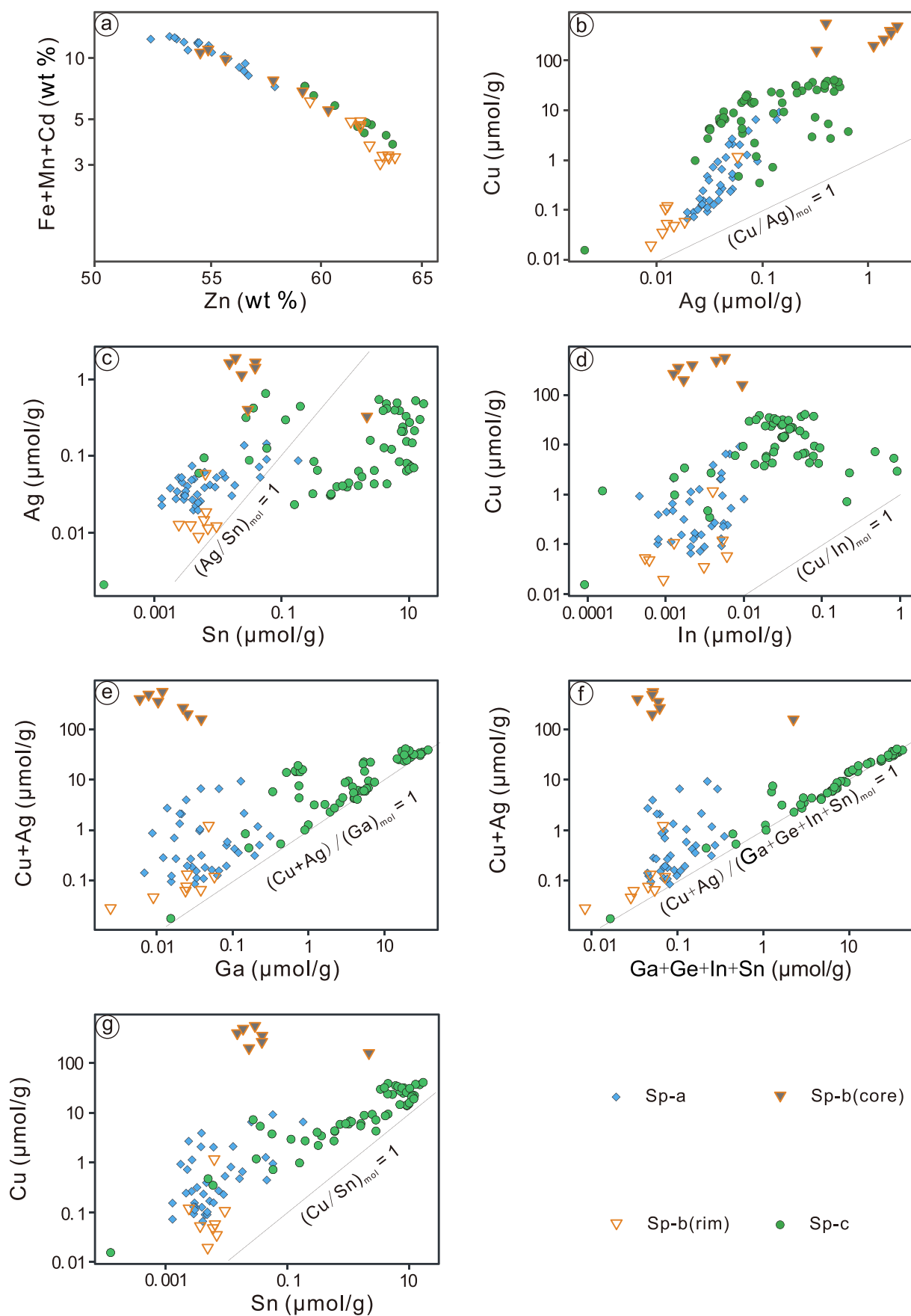


**Fig. 8.** Correlation plots of (a) Fe + Mn + Cd vs. Zn (b) Cu vs. Ag (c) Ag vs. Sn (d) Cu vs. In (e) Cu + Ag vs. Ga (f) Cu + Ag vs. Ga + Ge + Sn + In, and (g) Cu vs. Sn for the three types of sphalerites datasets. Dotted lines show the theoretical 1:1 correlation.

MS spot analysis (Fig. 6). Copper content is much higher in the Sp-b core than the rim (Fig. 6). The Sp-b rims are compositionally similar to Sp-a, as supported by the PCA plot (Fig. 7c).

The results from LA-ICPMS (Supplementary Table S2) are consistent with those from EPMA. The trace element contents of the Qixiashan sphalerite grains are presented in Table 1 and Supplementary Table S2. A total of 110 analyses were conducted (euhedral black Sp-a:  $n = 39$ ; zoned Sp-b from rim to core:  $n = 15$ ; and light color Sp-c:  $n = 56$ ). Indium, Sn, Ge, and Sb contents are below the LA-ICP-MS detection limit for all three types of sphalerites. The Sp-a grains have high Fe and Mn concentrations, while Sp-c has high Ga, Cu, Cd, Sn, and Ag contents, 1 to 2 orders of magnitude above Sp-a (Table A1). The Ag content show small variations within the same type of sphalerite. The concentrations of Fe, Cu, Mn, Ag, and Pb in the core is much higher than in the rim of a single Sp-b grain, while there is no major core-rim difference for Cd content (Table A1, Table 1).

For Sp-a, positive correlations are found in Fe-In, Fe-Ga, Cu-Ag, Ag-Sn and Cu-Pb, while negative correlations exist in Fe-Cd and Ga-Cd (Supplementary Fig. S1). For the Sp-b core, positive correlations were found in Fe-Cu, In-Sn, In-Mn, Sn-Mn, Sn-Ga and Cd-Ga, and negative correlations in Fe-Ga, Cu-Ga, Pb-Ag, Cd-Ag (Supplementary Fig. S3). For the Sp-b rim, positive correlations are present in Fe-Mn, Cu-Ag, Pb-Ag and Cu-Pb, whereas negative correlations in Fe-Cd and Mn-Cd (Supplementary Fig. S4). For, Sp-c, positive correlations were found in Fe-Mn, Fe-Cd, Cu-Ag, Cu, Ga, Cu-Sn, Ag-Ga, Ag-As, and As-Pb (Supplementary Fig. S2).

The  $\delta^{34}\text{S}$  values of 11 Qixiashan sphalerite and galena samples ( $-3.7$  to  $+7.8\%$ ;  $n = 68$ ) are listed in Supplementary Table S3 and summarized in Tables 1 and 2. The six sphalerite samples have similar  $\delta^{34}\text{S} = -1.7$  to  $+7.8\%$  (Sp-a:  $+1.0$  to  $+7.4\%$ , Sp-b:  $+3.1$  to  $+7.8\%$ , Sp-c:  $-1.7$  to  $+6.5\%$ ;  $n = 48$ ). The  $\delta^{34}\text{S}$  values vary across the zoned Sp-b, increasing from the core ( $+3.1$  to  $+5.6\%$ ) to rim ( $+4.2$  to  $+7.8\%$ ). The seven galena samples have  $\delta^{34}\text{S} = -3.7$  to  $+3.0\%$  ( $n = 20$ ).

The PCA results are shown in Fig. 7. The first principal component (PC1) occupies 42.0% of the variance contribution rate, with the eigenvalue of 4.62. PC1 is a measure of the Cu, Ag, Ga, Cd, In, and Ge concentrations (Fig. 7a and b). PC2 accounts for 24.8% of the total variance, with the eigenvalue of 2.73. It is a measure of the Mn, Fe and Pb concentrations (Fig. 7a and b).

## 6. Discussion

### 6.1. Element substitution mechanism

Sphalerite can incorporate many metals into its structure, including Fe, In, Ge, Ga, Cd, Mn, Hg, Cu, Co, and Ni (Cook et al., 2009; Ye et al., 2011; Murakami and Ishihara, 2013; Lockington et al., 2014; Frenzel et al., 2016; Bauer et al., 2019a; Bauer et al., 2019b; Xu et al., 2021; Yu et al., 2020). Varying concentration and valence state of these metals are linked to different incorporation processes during sphalerite growth (Belissont et al., 2014). Bivalent cations ( $\text{Cu}^{2+}$ ,  $\text{Ni}^{2+}$ ,  $\text{Co}^{2+}$ ,  $\text{Fe}^{2+}$ ,  $\text{Mn}^{2+}$ ,  $\text{Ge}^{2+}$  and  $\text{Cd}^{2+}$ ) have ionic radii similar to that of  $\text{Zn}^{2+}$ . These ions are incorporated in sphalerite via simple substitution for  $\text{Zn}^{2+}$  (Bonnet et al., 2016), as expressed by:



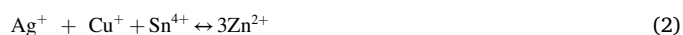
Strong (Fe + Mn + Cd) vs. Zn correlation suggest direct substitution of ( $\text{Fe}^{2+}$ ,  $\text{Mn}^{2+}$ ,  $\text{Cd}^{2+}$ )  $\leftrightarrow \text{Zn}^{2+}$  in the Qixiashan sphalerite (Fig. 8a). In contrast, large variation in Cu contents is present within different types of sphalerite, indicating that the Cu enrichment is associated with different crystallization conditions (e.g., temperature) and Cu ( $\text{Cu}^+$  or  $\text{Cu}^{2+}$ ) incorporation mechanism (Pfaff et al., 2011; Bonnet et al., 2016). Sphalerite accommodates Cu mainly as: (1) solid solution; or (2) chalcopyrite disease (Barton and Bethke, 1987). In the former case,  $\text{Cu}^+$  and  $\text{Ag}^+$  provide charge compensation to enhance tri- and tetravalent

**Table 3**

Calculated temperatures of sphalerite with GGIMFis.

Sphalerite	Temperature (°C)		Ga	Ge	Fe	Mn	In
Type	Range	Mean	(ppm)	(ppm)	(wt%)	(ppm)	(ppm)
Sp-a	274–315	294	4.54	2.23	4.63	2724	0.41
Sp-b (rim)	285–307	296	1.66	0.69	2.08	2435	0.30
Sp-b (core)	321–348	333	1.21	0.68	5.27	4746	0.43
Sp-b (rim)	286–314	299	2.32	0.65	2.14	2014	0.30
Sp-c	146–255	203	600	2.26	1.09	402	8.92

cations ( $\text{In}^{3+}$ ,  $\text{Sn}^{3+}$  and  $\text{Sn}^{4+}$ ) substitution for Zn (Cook et al., 2009; Ye et al., 2011). The positive Ag vs. Cu (Fig. A1) and Ag vs. Sn (Fig. A1) correlations with a trend sub-parallel to the molar ratio ( $\text{Ag}/\text{Cu}$ ) mol = 1 and ( $\text{Ag}/\text{Sn}$ ) mol = 1 of Sp-a (Fig. 8b and c), suggesting a coupled substitution in Sp-a (Cook et al., 2009):



The data points of (Cu vs In) are not distributed along the ( $\text{Cu}/\text{In}$ )<sub>mol</sub> = 1:1 line (cf. Fig. 8d), supporting that  $2\text{Zn}^{2+} \leftrightarrow \text{Cu}^+ + \text{In}^{3+}$  does not occur. Most of the data points deviate from the ( $\text{Cu}/\text{In}$ )<sub>mol</sub> = 1 line ( $\text{Cu}/\text{In} > 1$ ; Fig. 8d). Another coupled substitution probably occurs because monovalent  $\text{Cu}^+$  (and  $\text{Ag}^+$ ) commonly correlates with  $\text{Ga}^{3+}$  (Bonnet et al., 2016):



Given the high Ga concentration and positive Ga vs. Cu correlation (Fig. A2), we used the  $\text{Ga}^{3+}$  vs. ( $\text{Cu}^+ + \text{Ag}^+$ ) plot (Fig. 8e) to determine whether reaction [3] had occurred. Most of the Sp-c data points plot along the ( $\text{Cu} + \text{Ag})/\text{Ga} = 1:1$  line, suggesting that reaction [3] had occurred. This is also supported by PCA results that Cu, Ag and Ga are measured by PC1 (Fig. 7). Despite that some Sp-a and Sp-b (rim) data points fall along the ( $\text{Cu} + \text{Ag})/\text{Ga} = 1:1$  line, the lack of correlation between those elements in Sp-a and Sp-b (Figs. A1, A3, A4) exclude the coupled substitution of Eq. [3] in these sphalerites.

The strong (Cu + Ag) vs. (Ga + Ge + In + Sn) correlation (tri- and tetravalent cations) along the 1/1 M ratio (Figs. 7 and 8f) highlights a general coupled substitution mechanism for Cu and other trace elements in sphalerite, substituting for Zn (e.g., Belissont et al., 2014; Cook et al., 2009). This is also supported by the positive correlations in Cu vs. Ag (Sp-a and Sp-b (rim)), Cu vs. In, and Cu vs. Sn in Sp-a (Fig. A1).

The high Cu/In of Sp-b (core) data (Fig. 8f) related to widespread chalcopyrite disease (Barton and Bethke, 1987), since the Cu concentration in Sp-b (core) exceeds the solubility limit in the Cu-Fe-Zn-S system ( $\sim 1.6$  wt% at 300 °C; Kojima and Sugaki, 1985). The positive Fe vs. Cu support that chalcopyrite disease ( $\text{CuFeS}_2$ ) had formed (Fig. A3). The Cu vs. Fe correlation in the Sp-b core represents mixed analyses (Fig. A3).

Other elements (e.g., Cu and Sn) in Sp-c (Fig. 8g) support the coupled substitution  $\text{Ag}^+ + \text{Cu}^+ + \text{Sn}^{4+} \leftrightarrow 3\text{Zn}^{2+}$ , since Sp-c data points fall along the ( $\text{Cu}/\text{Sn}$ )<sub>mol</sub> = 1 line.

### 6.2. Sphalerite formation temperature

The sphalerite minor and trace element compositions are related to its deposition conditions (e.g., temperature and redox) and fluid composition (Cook et al., 2009; Frenzel et al., 2016; Bonnet et al., 2016; Bauer et al., 2019b). The GGIMFis geothermometer for Ga, Ge, In, Mn, and Fe in sphalerite was proposed by Frenzel et al. (2016), and supported by Bauer et al. (2019a).

In this study, we calculated the temperatures of the three types of sphalerites with the GGIMFis geothermometer (Table 3), and the results are consistent with the fluid inclusion homogenization temperature (182–348 °C; Sun et al., 2019). Our results indicate that the formation temperature of Sp-a (294 °C) is higher than that of Sp-c (203 °C), which would promote Fe and Mn substitution for Zn in Sp-a. Meanwhile, the

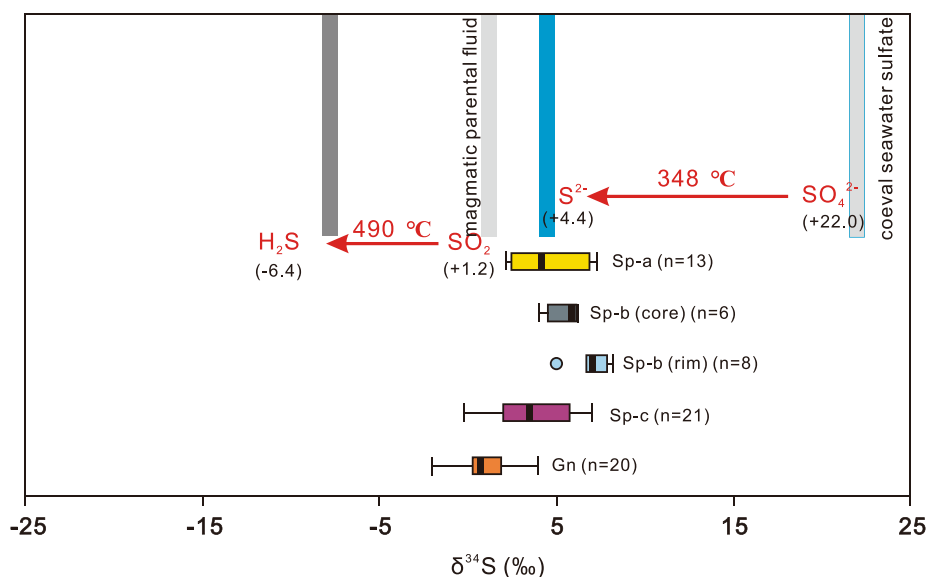


**Fig. 9.** Thermodynamic equilibrium fractionation of S isotope for potential sulfur source. Equilibrium fractionation factors of sulfur between  $\text{SO}_2$  and  $\text{H}_2\text{S}$  are from Ohmoto and Rye (1979), and the equilibrium fractionation factors of sulfur between sulfate- $\text{S}^{2-}$  are from Ohmoto and Lasaga (1982).

lower-temperature crystallization of Sp-c may have enriched Ga, Cu, and Ag. This is supported by PCA results that Fe and Mn show positive in Sp-a, while Sp-c has Ga, Cu, and Ag affinity (Fig. 7). This finding is consistent with previous studies that high-temperature sphalerite could incorporate more Fe and Mn than its low-temperature counterparts (Cook et al., 2009; Ye et al., 2011; Keith et al., 2014; Belissont et al., 2014; Bauer et al., 2019b).

The zoned Sp-b has higher temperature in the core (~330 °C) than the rim (296–299 °C), indicating that cooling during its crystallization. The extensive chalcopyrite disease in Sp-b core is probably in response to the extremely high temperature (~330 °C) during initial Sp-b crystallization.

### 6.3. Sulfur source and migration pathway

Previous studies considered the sediment-hosted Pb-Zn deposits in the Carboniferous limestone in MLYRB to have had a magmatic-hydrothermal origin (e.g., Xinqiao, Li et al., 2018). To test this hypothesis in Qixiashan, we assume that the  $\delta^{34}\text{S}_{\text{fluid}} = +1.2\text{‰}$  (from the nearby Anjishan skarn-porphyry Cu deposit in Ningzhen; Zhang, 1992) as the initial sulfur reservoir for the Qixiashan Pb-Zn-Fe system. We calculated the expected  $\delta^{34}\text{S}$  range for equilibrium fractionation of sphalerite from magmatic water at 490 °C (temperature of early magmatic assemblages from Anjishan; Zhang 1992). Using the fractionation factors of Ohmoto and Rye (1979), a 490 °C  $\text{SO}_2$ -rich fluid with  $\delta^{34}\text{S} = +1.2\text{‰}$  (Zhang, 1992) would produce an  $\text{H}_2\text{S}$  gas with  $\delta^{34}\text{S} = -6.4\text{‰}$  (Fig. 9), which would in turn produce sphalerite and galena with  $\delta^{34}\text{S} = -6.1$  to  $-5.9\text{‰}$  and  $-9.1$  to  $-8.3\text{‰}$ , respectively (based on the calculated temperature with GGIMFis). The measured  $\delta^{34}\text{S}$  values for all types of sphalerites ( $-1.7$  to  $+7.8\text{‰}$ ) and galena ( $-3.7$  to  $+3.0\text{‰}$ ) at Qixiashan are higher than the equilibrium fractionation products of magmatic parental fluid (Fig. 9). Thus, those measured  $\delta^{34}\text{S}$  values cannot be explained only by the  $\delta^{34}\text{S}$  change of the fluid during crystal growth. In addition, the  $\delta^{34}\text{S}$  variation may have caused by changes in  $f\text{O}_2$  and pH, and by fluid mixing and sulfur disproportionation (Tanner et al., 2016). Furthermore, the Qixiashan deposit is neither associated with plutonic bodies nor magmatic-hydrothermal alteration, which suggest that the sulfur was unlikely sourced from magmatic-derived fluid.

A potential reservoir of  $^{34}\text{S}$ -rich sulfur is the Paleozoic–Lower Mesozoic evaporites in the MLYRB ( $+22\text{‰}$ ; Pan and Dong, 1999).

Assuming an equilibrium fractionation from a seawater sulfate-bearing fluids, and using the fluid inclusion homogenization temperatures from the Qixiashan sphalerite (182–348 °C; Sun et al., 2019) and the calculated temperature via GGIMFis (146–348 °C), the initial hydrothermal fluid (348 °C with  $\delta^{34}\text{S} = +22\text{‰}$ ) would produce  $\text{S}^{2-}$  with  $\delta^{34}\text{S} = +4.4\text{‰}$  (Ohmoto and Lasaga, 1982; Fig. 9). This value is consistent with the measured  $\delta^{34}\text{S}$  for the Qixiashan sphalerite and galena ( $-3.7$  to  $+7.8\text{‰}$ ; Fig. 9). Therefore, the ore sulfur may have sourced from seawater sulfate through a higher temperature associated thermochemical sulfate reduction (TSR). Furthermore, the negative  $\delta^{34}\text{S}$  values of layered pyrite ( $-27.4$  to  $-23.1\text{‰}$ ; Nanjing Yinmao Lead & Zinc Mining Co., 2016) preserved a sulfate-unlimited open system, which indicates adequate sulfate pool to provide sufficient  $\text{S}^{2-}$  for the ore sphalerite and galena (Seal, 2006).

### 6.4. Implications for regional Pb-Zn mineralization

Gu et al. (2007) suggested that the Fe and Mn of massive sulfide orebodies in the MLYRB were sourced from Early Carboniferous submarine exhalation. The Carboniferous sedimentary sulfide layer (dominated by massive pyrite) has been proposed by Xu and Zhou (2001) to be a prerequisite for the subsequent hydrothermal mineralization in the MLYRB. Li et al. (2018) concluded that preexisting sulfide layer in Carboniferous carbonate rocks contributed Cu and Au to the Cretaceous MLYRB mineralization. Similarly, pre-existing pyrites and sediments of the Qixiashan deposit is a potential source for the subsequent local mineralization.

We consider that higher Fe and Mn in Sp-a derived from syn-sedimentary to early-diagenetic mineralization, as supported by the diagenetic origin of pyrites with high Mn and low Co/Ni contents (author's unpublished data). The Pb-Zn (from basement, Pb isotope evidence; Zhang et al., 2017) hydrothermal fluid may have flowed through the sediments and preexisting massive sulfide layer in Huanglong Formation (i.e., pre-ore pyrites of Qixiashan) and leached out the metals (Fe and Mn), which eventually formed the Fe-Mn-bearing Sp-a. Its sulfur was sourced from the ambient seawater sulfate, because thermochemical sulfate reduction (TSR) is associated with deposition of carbonate minerals and higher temperature ( $>100$  °C; Gadd et al., 2017; Rajabi et al., 2020). The siderite coexisting with Sp-a (Fig. 5c and d) supports the TSR origin of reduced sulfur for Sp-a (Fig. 9).

The Sp-b Fe-rich and Zn-depleted core contains chalcopyrite

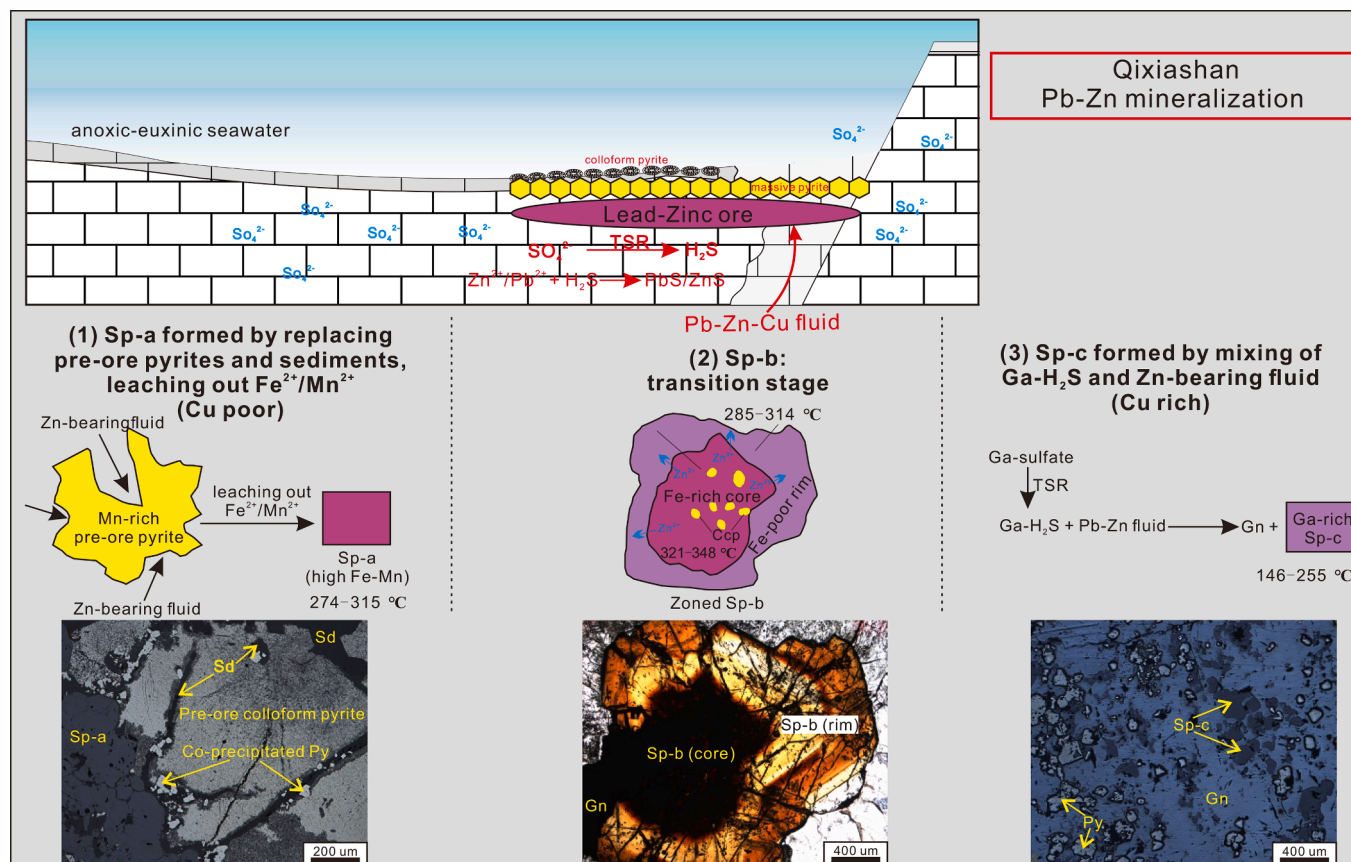


**Fig. 10.** Schematic diagram for the Pb-Zn mineralization at Qixiashan. High-temperature black sphalerite (Sp-a) was formed when the ore fluid flowed through and replaced the pre-ore pyrite layer and sediments, and inherited the Fe and Mn from the latter. Zoned Sp-b formed during the transition stage that from Cu poor (Sp-a) to Cu rich (Sp-c) fluids. The light-color Ga-rich sphalerite (Sp-c) precipitated by mixing of Ga- $\text{H}_2\text{S}$  (reduced from sulfate) and epigenetic Zn-bearing fluid.

inclusions, surrounded by a Fe-poor, Zn rich and chalcopyrite free rim (Fig. 6). The Sp-b rims are compositionally similar to Sp-a, as supported by the PCA plot (Fig. 7c). Therefore, zoned Sp-b possibly represents the transition stage from poor copper (Sp-a) to rich copper (Sp-c) fluids.

Light-color Sp-c was likely formed in a low-temperature Ga-Cu-Cd-Sn-Ag-rich and Fe-Mn-poor fluid. The elevated Ga contents in Sp-c suggests that coeval ore-forming fluids contain hydroxide, fluoride, or sulfate, which could form stable complexes with Ga (Wood and Samson, 2006). Therefore, Sp-c was possibly formed by the mixing of Ga- $\text{H}_2\text{S}$  and Zn-bearing fluids (Fig. 10). The Ga-sulfate was reduced to hydrogen sulfide via TSR, then mixing with Zn-/Pb-bearing fluid to precipitate galena and Sp-c. The decreasing  $\delta^{34}\text{S}$  values from Sp-a to Sp-c indicate a more oxidizing condition during late metallogenic stage, and thus sphalerite can incorporate more tri- and tetravalent cations.

## 7. Conclusions

This study demonstrates that the sphalerite minor and trace element compositions and the sulfide S-isotopes reflect distinctive ore-forming processes. High-temperature black sphalerite (Sp-a) was formed when Pb-Zn hydrothermal fluid flowed through and replaced the preexisting sulfide layer or sediments (i.e., pre-ore pyrites of Qixiashan), which leached out the metals (Fe and Mn) and then incorporated them into the Sp-a structure. Sp-b represents the transition stage from poor copper (Sp-a) to rich copper (Sp-c) fluids. The light-color Ga-Cu-rich sphalerite (Sp-c) was possibly precipitated by mixing of Ga- $\text{H}_2\text{S}$  (reduced from sulfate) and epigenetic Zn-bearing fluid. We propose that the Qixiashan Pb-Zn mineralization has an epigenetic origin, with its ore sulfur sourced from seawater sulfate through thermochemical sulfate reduction (TSR).

## Declaration of Competing Interest

The authors declare that they have no known competing financial interests or personal relationships that could have appeared to influence the work reported in this paper.

## Acknowledgments

Editor-in-Chief Huayong Chen, and two anonymous reviewers are thanked for their constructive comments and suggestions, which helped improve this paper. The study was supported by the National Natural Science Foundation of China (41873043 and 42073001), the Project of Innovation-driven Plan of Central South University (2019CX035), the Open Research Fund Program of State Key Laboratory of Mineral Deposits Research (Nanjing University) (2018LAMDK02), and the Open Sharing Fund for the Large-scale Instruments and Equipment of Central South University (CSUZC202137).

## Appendix A. Supplementary data

Supplementary data to this article can be found online at <https://doi.org/10.1016/j.oregeorev.2022.104786>.

## References

- Anderson, G. M., 1983, Some geochemical aspects of sulfide precipitation in carbonate rocks: James Cook University of North Queensland.
- Barton, P.B., Bethke, P.M., 1987. Chalcopyrite disease in sphalerite; pathology and epidemiology. *American Mineralogist* 72, 451–467.
- Bauer, M.E., Seifert, T., Burisch, M., Krause, J., Richter, N., Gutzmer, J., 2019a. Indium-bearing sulfides from the Hämmerlein skarn deposit, Erzgebirge, Germany: evidence for late-stage diffusion of indium into sphalerite. *Mineralium Deposita* 54, 175–192.



- Bauer, M.E., Burisch, M., Ostendorf, J., Krause, J., Frenzel, M., Seifert, T., Gutzmer, J., 2019b. Trace element geochemistry of sphalerite in contrasting hydrothermal fluid systems of the Freiberg district, Germany: insights from LA-ICP-MS analysis, near-infrared light microthermometry of sphalerite-hosted fluid inclusions, and sulfur isotope geochemistry. *Miner Deposita* 54 (2), 237–262.
- Belissant, R., Boiron, M.-C., Luais, B., Cathelineau, M., 2014. LA-ICP-MS analyses of minor and trace elements and bulk Ge isotopes in zoned Ge-rich sphalerites from the Noailhac – Saint-Salvy deposit (France): Insights into incorporation mechanisms and ore deposition processes. *Geochimica et Cosmochimica Acta* 126, 518–540.
- Bonnet, J., Mosser-Ruck, R., Caumon, M.-C., Rouer, O., Andre-Mayer, A.-S., Cauzid, J., Peiffert, C., 2016. Trace Element Distribution (Cu, Ga, Ge, Cd, and Fe) in Sphalerite from the Tennessee Mvt Deposits, Usa, By Combined Empa, La-icp-ms, Raman Spectroscopy, and Crystallography. *The Canadian Mineralogist* 54 (5), 1261–1284.
- Carne, R., and Cathro, R., 1982, Sedimentary exhalative (sedex) zinclead-silver deposits, northern Canadian Cordillera: Canadian Institute of Mining Bulletin, p. 75:.
- Cook, N.J., Ciobanu, C.L., Pring, A., Skinner, W., Shimizu, M., Danyushevsky, L., Saini-Eidukat, B., Melcher, F., 2009. Trace and minor elements in sphalerite: A LA-ICPMS study. *Geochimica et Cosmochimica Acta* 73 (16), 4761–4791.
- Corbella, M., Ayora, C., Cardellach, E., 2004. Hydrothermal mixing, carbonate dissolution and sulfide precipitation in Mississippi Valley-type deposits. *Mineralium Deposita* 39 (3), 344–357.
- Frenzel, M., Hirsch, T., Gutzmer, J., 2016. Gallium, germanium, indium, and other trace and minor elements in sphalerite as a function of deposit type — A meta-analysis. *Ore Geology Reviews* 76, 52–78.
- Gadd, M.G., Layton-Matthews, D., Peter, J.M., Paradis, S., Jonasson, I.R., 2017. The world-class Howard's Pass SEDEX Zn-Pb district, Selwyn Basin, Yukon. Part II: the roles of thermochemical and bacterial sulfate reduction in metal fixation: *Mineralium Deposita* 52 (3), 405–419.
- Gao, S., Ling, W., Qiu, Y., Lian, Z., Hartmann, G., Simon, K., 1999. Contrasting geochemical and Sm-Nd isotopic compositions of Archean metasediments from the Kongling high-grade terrain of the Yangtze craton: evidence for cratonic evolution and redistribution of REE during crustal anatexis. *Geochimica et Cosmochimica Acta* 63 (13–14), 2071–2088.
- Gu, L., Khin Zaw, Hu, W., Zhang, K., Ni, P., He, J., Xu, Y., Lu, J., Lin, C., 2007. Distinctive features of Late Palaeozoic massive sulphide deposits in South China. *Ore Geology Reviews* 31 (1–4), 107–138.
- Guo, WeiMin, Lu, JianJun, Jiang, ShaoYong, Zhang, RongQing, Qi, L., 2011. Re-Os isotope dating of pyrite from the footwall mineralization zone of the Xinqiao deposit, Tongling, Anhui Province: Geochronological evidence for submarine exhalative sedimentation. *Chinese Science Bulletin* 56 (35), 3860–3865.
- Hu, Z., Zhang, W., Liu, Y., Gao, S., Li, M., Zong, K., Chen, H., Hu, S., 2015. "Wave" signal-smoothing and mercury-removing device for laser ablation quadrupole and multiple collector ICPMS analysis: application to lead isotope analysis. *Analytical Chemistry* 87 (2), 1152–1157.
- Keith, M., Haase, K.M., Schwarz-Schampera, U., Klemm, R., Petersen, S., Bach, W., 2014. Effects of temperature, sulfur, and oxygen fugacity on the composition of sphalerite from submarine hydrothermal vents. *Geology* 42 (8), 699–702.
- Kelley, K.D., Leach, D.L., Johnson, C.A., Clark, J.L., Fayek, M., Slack, J.F., Anderson, V. M., Ayuso, R.A., Ridley, W.L., 2004. Textural, compositional, and sulfur isotope variations of sulfide minerals in the Red Dog Zn-Pb-Ag deposits, Brooks Range, Alaska: Implications for ore formation. *Economic Geology* 99 (7), 1509–1532.
- Kojima, S., and Sugaki, A., 1985, Phase relations in the Cu-Fe-Zn-S system between 500 degrees and 300 degrees C under hydrothermal conditions: *Economic Geology*, v. 80, p. 158–171.
- Li, K., Pring, A., Etschmann, B., Macmillan, E., Ngothai, Y., O'Neill, B., Hooker, A., Mosselmans, F., Brugger, J., 2015. Uranium scavenging during mineral replacement reactions. *American Mineralogist* 100 (8–9), 1728–1735.
- Li, X.-H., Li, W.-X., Wang, X.-C., Li, Q.-L., Liu, Y.-u., Tang, G.-Q., Gao, Y.-Y., Wu, F.-Y., 2010. SIMS U-Pb zircon geochronology of porphyry Cu-Au-(Mo) deposits in the Yangtze River Metallogenic Belt, eastern China: magmatic response to early Cretaceous lithospheric extension. *Lithos* 119 (3–4), 427–438.
- Li, Y., Li, J.-W., Li, X.-H., Selby, D., Huang, G.-H., Chen, L.-J., Zheng, K., 2017. An Early Cretaceous carbonate replacement origin for the Xinqiao stratabound massive sulfide deposit, Middle-Lower Yangtze Metallogenic Belt, China: *Ore Geology Reviews* 80, 985–1003.
- Li, Y., Selby, D., Li, X.-H., and Ottley, C. J., 2018, Multisourced metals enriched by magmatic-hydrothermal fluids in stratabound deposits of the Middle-Lower Yangtze River metallogenic belt, China: *Geology*, v. 46, p. 391–394 (in Chinese with English Abstract).
- Li, Y., Li, Q.-L., Yang, J.-H., 2019. Tracing water-rock interaction in carbonate replacement deposits: A SIMS pyrite S-Pb isotope perspective from the Chinese Xinqiao system. *Ore Geology Reviews* 107, 248–257.
- Li, Y., Yuan, F., Jowitt, S.M., Wang, F., Li, X., Deng, Y., Wang, Y., Zhou, T., 2021. Molybdenite Re-Os, titanite and garnet U-Pb dating of the Magushan skarn Cu-Mo deposit, Xuancheng district, Middle-Lower Yangtze River Metallogenic Belt: *Geoscience Frontiers* 12 (3), 101116. <https://doi.org/10.1016/j.gsf.2020.11.013>.
- Liu, W., Spinks, S.C., Glenn, M., MacRae, C., Pearce, M.A., 2021. How carbonate dissolution facilitates sediment-hosted Zn-Pb mineralization. *Geology* 49, 1363–1368.
- Liu, Y., Hu, Z., Gao, S., Günther, D., Xu, J., Gao, C., Chen, H., 2008. In situ analysis of major and trace elements of anhydrous minerals by LA-ICP-MS without applying an internal standard. *Chemical Geology* 257 (1–2), 34–43.
- Lockington, J.A., Cook, N.J., Ciobanu, C.L., 2014. Trace elements in sphalerites from the Mississippi Valley type lead zinc deposits around the margins of Yangtze Block and its geological implications : A LA-ICPMS study. *Mineralogy and Petrology* 108, 873–890.
- Magnall, J. M., Gleeson, S. A., and Paradis, S., 2020, A NEW SUBSEAFLOOR REPLACEMENT MODEL FOR THE MACMILLAN PASS CLASTIC-DOMINANT Zn-Pb ± Ba DEPOSITS (YUKON, CANADA): *Economic Geology*, v. 115, p. 953–959.
- Mao, J., Wang, Y., Lehmann, B., Yu, J., Du, A., Mei, Y., Li, Y., Zang, W., Stein, H.J., Zhou, T., 2006. Molybdenite Re-Os and albite 40Ar/39Ar dating of Cu-Au-Mo and magnetite porphyry systems in the Yangtze River valley and metallogenic implications. *Ore Geology Reviews* 29 (3–4), 307–324.
- Mao, J., Xie, G., Duan, C., Pirajno, F., Ishiyama, D., Chen, Y., 2011. A tectono-genetic model for porphyry-skarn-stratabound Cu-Au-Mo-Fe and magnetite-apatite deposits along the Middle-Lower Yangtze River Valley. *Eastern China: Ore Geology Reviews* 43 (1), 294–314.
- Mudd, G.M., Jowitt, S.M., Werner, T.T., 2017. The world's lead-zinc mineral resources: scarcity, data, issues and opportunities. *Ore Geology Reviews* 80, 1160–1190.
- Murakami, H., Ishihara, S., 2013. Trace elements of Indium-bearing sphalerite from tin-polymetallic deposits in Bolivia. China and Japan: A femto-second LA-ICPMS study: *Ore Geology Reviews* 53, 223–243.
- Nanjing Yinmao Lead & Zinc Mining Co., 2016, Replacement resource survey report of Qixiashan Pb-Zn deposit, Nanjing, Jiangsu Province, China (in Chinese): unpublished (in Chinese).
- Ohmoto, H., Lasaga, A.C., 1982. Kinetics of reactions between aqueous sulfates and sulfides in hydrothermal systems. *Geochimica et Cosmochimica Acta* 46 (10), 1727–1745.
- Ohmoto, H., Rye, R., 1979. Isotopes of sulfur and carbon: *Geochemistry of hydrothermal ore deposits*: New York. John Wiley 509–567.
- Pan, Y., Dong, P., 1999. The Lower Changjiang (Yangzi/Yangtze River) metallogenic belt, east central China: intrusion-and wall rock-hosted Cu-Fe-Au, Mo, Zn, Pb, Ag deposits: *Ore Geology Reviews* 15 (4), 177–242.
- Pfaff, K., Koenig, A., Wenzel, T., Ridley, I., Hildebrandt, L.H., Leach, D.L., Markl, G., 2011. Trace and minor element variations and sulfur isotopes in crystalline and colloform ZnS: Incorporation mechanisms and implications for their genesis. *Chemical Geology* 286, 118–134.
- Pirajno, F., Zhou, T., 2015. Intracrustal porphyry and porphyry-skarn mineral systems in Eastern China: scrutiny of a special case "Made-in-China". *Economic Geology* 110 (3), 603–629.
- Polito, P.A., Kyser, T.K., Golding, S.D., Southgate, P.N., 2006. Zinc deposits and related mineralization of the Burketown mineral field, including the world-class Century deposit, northern Australia: Fluid inclusion and stable isotope evidence for basin fluid sources. *Economic Geology* 101 (6), 1251–1273.
- Rajabi, A., Alfonso, P., Canet, C., Rastad, E., Niroomand, S., Modabberi, S., Mahmoodi, P., 2020. The world-class Koushk Zn-Pb deposit, Central Iran: A genetic model for vent-proximal shale-hosted massive sulfide (SHMS) deposits – Based on paragenesis and stable isotope geochemistry. *Ore Geology Reviews* 124, 103654. <https://doi.org/10.1016/j.oregeorev.2020.103654>.
- Rye, R. O., and Ohmoto, H., 1974, Sulfur and Carbon Isotopes and Ore Genesis: A Review: *Economic Geology*, v. 69, p. 826–842.
- Seal, R.R., 2006. Sulfur Isotope Geochemistry of Sulfide Minerals. *Reviews in Mineralogy and Geochemistry* 61 (1), 633–677.
- Spinks, S. C., Pearce, M. A., Liu, W., Kunzmann, M., Ryan, C. G., Moorhead, G. F., Kirkham, R., Blaikie, T., Sheldon, H. A., Schaub, P. M., and Rickard, W. D. A., 2021, Carbonate Replacement as the Principal Ore Formation Process in the Proterozoic McArthur River (HYC) Sediment-Hosted Zn-Pb Deposit, Australia: *Economic Geology*, v. 116, p. 693–718.
- Sun, X., Ni, P., Chi, Z., Yang, Y., Jing, S., and Wang, G., 2019, The feature and evolution of ore forming fluid of Qixiashan Pb-Zn deposit, Nanjing: Constraints from fluid inclusion and H-O isotope: *Acta Petrologica Sinica*, v. 35, p. 3749–3762 (in Chinese with English Abstract).
- Sun, X.-J., Ni, P., Yang, Y.-L., Qin, H., Chen, H., Gui, C.-J., Jing, S., 2018. Formation of the Qixiashan Pb-Zn deposit in Middle-Lower Yangtze River Valley, eastern China: Insights from fluid inclusions and in situ LA-ICP-MS sulfur isotope data. *Journal of Geochemical Exploration* 192, 45–59.
- Tanner, D., Henley, R.W., Mavrogenes, J.A., Holden, P., 2016. Sulfur isotope and trace element systematics of zoned pyrite crystals from the El Indio Au-Cu-Ag deposit, Chile. *Contributions to Mineralogy and Petrology* 171, 33.
- Tooth, B., Ciobanu, C.L., Green, L., O'Neill, B., Brugger, J., 2011. Bi-melt formation and gold scavenging from hydrothermal fluids: An experimental study. *Geochimica et Cosmochimica Acta* 75 (19), 5423–5443.
- Wilkinson, J., Hitzman, M., Archibald, S., Piercey, S., 2015. The Irish Zn-Pb orefield: the view from 2014: Current Perspectives on Zinc Deposits. *Irish Association for Economic Geology, Dublin*, pp. 59–72.
- Wood, S.A., Samson, I.M., 2006. The aqueous geochemistry of gallium, germanium, indium and scandium. *Ore Geology Reviews* 28 (1), 57–102.
- Xu, G., Zhou, J., 2001. The Xinqiao Cu-S-Fe-Au deposit in the Tongling mineral district, China: synorogenic remobilization of a stratiform sulfide deposit. *Ore Geology Reviews* 18 (1–2), 77–94.
- Xu, J., Cook, N.J., Ciobanu, C.L., Li, X., Kontonikas-Charos, A., Gilbert, S., Lv, Y., 2021. Indium distribution in sphalerite from sulfide-oxide-silicate skarn assemblages: a case study of the Dulong Zn-Sn-In deposit. *Miner Deposita* 56 (2), 307–324.
- Ye, L., Cook, N.J., Ciobanu, C.L., Yüping, L., Qian, Z., Tiegeng, L., Wei, G., Yulong, Y., Danyushevskiy, L., 2011. Trace and minor elements in sphalerite from base metal deposits in South China: A LA-ICPMS study. *Ore Geology Reviews* 39 (4), 188–217.
- Yu, D., Xu, D., Zhao, Z., Huang, Q., Wang, Z., Deng, T., Zou, S., 2020. Genesis of the Taolin Pb-Zn deposit in northeastern Hunan Province, South China: constraints from trace elements and oxygen-sulfur-lead isotopes of the hydrothermal minerals. *Mineralium Deposita* 55 (7), 1467–1488.
- Zeng, J., Li, J., Chen, J., and Lu, J., 2013, SHRIMP Zircon U-Pb Dating of Anjishan Intrusive Rocks in Ningzhen District, Jiangsu, and Its Geological Significance: *Earth*

- Science—Journal of China University of Geosciences, v. 38, p. 57-67 (in Chinese with English Abstract).
- Zeng, P., Pei, R., Hou, Z., Meng, Y., Yang, Z., Wang, X., Tian, S., Xu, W., and Jiang, Z., 2002, Sedex-type massive sulfide deposits in Tongling Block, Anhui: China, v. 21, p. 532–535.
- Zhang, J., 1992, Geological characters and metallogenic model of Anjishan copper deposit: Jiangsu Geology, v. 16, p. 172-179 (in Chinese with English Abstract).
- Zhang, M., Chen, R.-Y., Ye, T.-Z., Li, J.-C., Lv, Z.-C., He, X., Chen, H., and Yao, L., 2017, Genetic study on the Qixiashan Pb-Zn polymetallic deposit in Jiangsu Province: Evidence from fluid inclusions and H-O-S-Pb isotopes: Acta Petrologica Sinica, v. 33, p. 3453-3470 (in Chinese with English Abstract).
- Zhou, T., Wang, S., Fan, Y.u., Yuan, F., Zhang, D., White, N.C., 2015. A review of the intracontinental porphyry deposits in the Middle-Lower Yangtze River Valley metallogenic belt. Eastern China: Ore Geology Reviews 65, 433–456.